Origins of n-type doping difficulties in perovskite stannates

L. Weston, L. Bjaalie, K. Krishnaswamy, and C. G. Van de Walle

Phys. Rev. B **97**, 054112 — Published 26 February 2018

DOI: 10.1103/PhysRevB.97.054112

Origins of n-type doping difficulties in perovskite stannates

L. Weston, L. Bjaalie, K. Krishnaswamy, and C. G. Van de Walle
Materials Department, University of California Santa Barbara, California 93106-5050, USA
(Dated: January 2, 2018)

The perovskite stannates ($A\mathrm{SnO_3}$; A = Ba, Sr, Ca) are promising for oxide electronics, but control of n-type doping has proved challenging. Using first-principles hybrid density functional calculations, we investigate La dopants and explore the formation of compensating acceptor defects. We find that La on the A site always behaves as a shallow donor, but incorporation of La on the Sn site can lead to self-compensation. At low La concentrations and in O-poor conditions, oxygen vacancies form in $\mathrm{BaSnO_3}$. A-site cation vacancies are found to be dominant among the native compensating centers. Compared to $\mathrm{BaSnO_3}$, charge compensation is a larger problem for the wider-band-gap stannates, $\mathrm{SrSnO_3}$ and $\mathrm{CaSnO_3}$, a trend we can explain based on conduction-band alignments. The formation of compensating acceptor defects can be inhibited by choosing oxygen-poor (cation-rich) growth or annealing conditions, thus providing a pathway for improved n-type doping.

I. INTRODUCTION

The perovskite stannate $\mathrm{BaSnO_3}$ (BSO) has attracted significant attention due to reports of high n-type carrier mobilities.[1–3] Lanthanum-doped BSO single crystals exhibit a room-temperature electron mobility of 320 $\mathrm{cm^2V^{-1}s^{-1}}$,[3] significantly higher than that of other perovskite oxides. The high electron mobility originates from the dispersive electronic states around the conduction-band minimum (CBM), which have predominantly Sn 5s character, leading to a low electron effective mass[4] and reduced electron-phonon scattering rates.[5,6] The excellent transport properties are combined with an optical band gap greater than 3 eV,[7] and consequently BSO is a promising transparent conducting oxide (TCO).[8] Moreover, BSO may be combined with other perovskite oxides, giving access to the rich physics and functionality exhibited by the perovskites,[9,10] and offering the prospect of forming novel oxide-based devices.[4,11,12]

Lanthanum-doped BSO sometimes exhibits carrier concentrations less than expected for fully ionized $\mathrm{La_{Ba}}$ donors.[13–16] Previously, the role of extended defects in affecting carrier mobility and concentration in BSO has been emphasized.[14,17] However, more recently, Prakash *et al.* have shown that deviations from stoichiometry lead to a dramatic reduction in the concentration and mobility of n-type carriers, highlighting the role of compensating point defects in this material.[16] $\mathrm{La_{Ba}}$ donors could be compensated by acceptor-type native point defects (such as cation vacancies), or by $\mathrm{La_{Sn}}$ acceptors in a process of self-compensation.

Other alkaline-earth stannates such as $\mathrm{SrSnO_3}$ (SSO) and $\mathrm{CaSnO_3}$ (CSO) are also of interest; these materials are not only promising TCOs in their own right, but can be alloyed with BSO to provide tunability in the lattice constant and band gap.[18] BSO has a lattice constant of 4.12 Å[19] and exhibits a large lattice mismatch with commonly available oxide substrates such as $\mathrm{SrTiO_3}$ (which has a lattice constant of 3.91 Å). Such a lattice mismatch can lead to formation of extended defects and reduced electron moblility.[3] The (pseudocubic) lattice constants of SSO and CSO are smaller than those of BSO: a = 4.04 Å for SSO and a = 3.97 Å for CSO.[20] Alloying provides access to intermediate lattice constants. In addition, the band gaps of SSO and CSO are significantly larger than that of BSO, with the CBM being more than 1 eV higher in energy.[21] These materials and their alloys thus present great opportunities for band-offset and strain engineering in heterostructures.

Recently, thin films of SSO doped with La have been grown by molecular beam epitaxy (MBE),[18] and these films were reported to be insulating. $(\mathrm{Ba,Sr})\mathrm{SnO_3}$ alloys were also grown and doped with La,[18] and it was found that n-type conductivity could only be achieved for thin films with very low Sr content. Baba *et al.*[22] also studied n-type doping of SSO thin films with La; their films exhibited n-type conductivity, however with poor doping efficiency. Apparently, n-type doping is far more difficult in SSO than in BSO. To our knowledge, doping and defects have not been studied in CSO to date; we are including the material as part of our study in order to better eluciate trends and build understanding of the perovskite stannates in general.

In this work we use first-principles calculations based on hybrid density functional theory (DFT) to investigate the origins of n-type doping difficulties in alkaline-earth stannates ($A\mathrm{SnO_3}$; A = Ba, Sr, Ca). One focus of our study is the La dopant itself. $\mathrm{La_{Ba}}$ has been shown to be a shallow donor in BSO,[23] but it is conceivable it could be a deep donor in SSO and CSO. We therefore explore the nature of the donor state. In addition, La may incorporate on a Sn site, where it acts as an acceptor. We also explore native point defects, focusing on those that act as acceptors and can hence act as compensating centers. The formation energies of all acceptor species become lower when the Fermi level is near the CBM, i.e., under n-type doping, and this can lead to compensation. We also discuss oxygen vacancies, since these can be an additional source of n-type carriers. Scanlon[23] reported a study of point defects in BSO; here we systematically extend this to SSO and CSO, and investigate the formation of compensating acceptor defects under different chemical conditions. We also analyze and explain the trends

in charge compensation across the $A\mathrm{SnO_3}$ series.

We find that the dominant compensating species are $\mathrm{La_{Sn}}$, which acts as an acceptor, and native A-site cation vacancies. Our caculations show that the issue of charge compensation is worse for SSO (and CSO) when compared to BSO, consistent with recent experiments.[18] The extent to which specific species contribute to compensation depends on growth or annealing conditions (expressed by chemical potentials in our study); in general we find that the formation of compensating acceptors is reduced under oxygen-poor conditions, and this provides a promising route to improving n-type doping in the perovskite stannates.

The manuscript is organized as follows. Our methodology is presented in Sec. II. Section III A contains results for the bulk materials. Results for La dopants and native defects are presented in Sec. III B and III C. The physics of compensation is examined in Secs. III D, III E, and III F; the dependence on La doping levels is examined in Sec. III G, and comparisons with eperiments are discussed in Sec. III H. Our key findings are summarised in Sec. IV.

II. METHODOLOGY

A. First-principles calculations

First-principles calculations are performed based on DFT with a hybrid functional, which provides reliable values for defect formation energies and transition levels in semiconductors and insulators.[24] We use the screened hybrid functional of Heyd, Scuseria and Ernzerhof (HSE),[25,26] as implemented within the Vienna *Ab-inito* Simulation Package.[27] The short-range exchange potential is calculated by mixing a fraction of nonlocal Hartree-Fock exchange with the generalized gradient approximation (GGA) of Perdew, Burke and Ernzerhof (PBE).[28] The long-range exchange potential and the correlation potential are calculated with the PBE functional. The screening length and mixing parameter are fixed at 10 Å and $\alpha = 0.25$, respectively.[29,30] As described in Sec. III F, we have checked the sensitivity of our results to the value of the mixing parameter. The valence electrons are separated from the core based on projector-augmented-wave (PAW) potentials.[31] An energy cut-off of 500 eV was used for the plane-wave basis set.

For the 5-atom cubic (BSO), and 20-atom orthorhombic (SSO, CSO) primitive cells, we use $6 \times 6 \times 6$ and $4 \times 4 \times 3$ k-point grids, respectively. Defect calculations were performed in a 135-atom $3 \times 3 \times 3$ supercell for BSO, and a 160-atom $2 \times 2 \times 2$ supercell for SSO and CSO. For these supercells we use a $2 \times 2 \times 2$ k-point grid. During the structural relaxations of the defect-containing supercells, the lattice constants were fixed to their corresponding bulk values, and the internal coordinates were relaxed until the Hellman-Feynman forces were less than 0.01 eV/Å. Spin polarization was taken into account.

B. Defect calculations

The formation energy of a defect D in charge state q is defined as[24]:

$$E^f(D^q) = E_{\mathrm{tot}}(D^q) - E_{\mathrm{tot}}(\mathrm{bulk}) - \sum_i n_i\mu_i + qE_F + \Delta^q\,, \tag{1}$$

where $E_{\mathrm{tot}}(D^q)$ is the total energy of a supercell containing D^q, and $E_{\mathrm{tot}}(\mathrm{bulk})$ is the total energy of the defect-free supercell; n_i is the number of atoms of species i ($i =$ Ba, Sr, Ca, Sn, O, La) added to ($n_i > 0$) and/or removed from ($n_i < 0$) the supercell to form the defect, and μ_i are the chemical potentials of the corresponding species; E_F is the Fermi level referenced to the valence-band maximum (VBM), and Δ^q is a correction term to align the electrostatic potential in the perfect bulk and defect supercells, and to account for finite-cell size effects on the total energies of charged defects, using the approach of Freysoldt *et al.*.[32,33]

In thermodynamic equilibrium, the concentration of a defect (c) is determined by the formation energy according to a Boltzmann expression:

$$c = N_{sites} \exp\left(\frac{-E^f[D^q]}{k_B T}\right), \tag{2}$$

where N_{sites} is the concentration of sites on which the defect can form, $E^f[D^q]$ is the formation energy [Eq. (1)], k_B is the Boltzmann constant, and T is the temperature. Consequently, if the conditions are close to equilibrium (which is the case in high-temperature growth or annealing), only defects with a sufficiently low formation energy will be present in large concentrations.

The charge-state transition level $\epsilon(q/q')$ is defined as the Fermi-level position below which the defect is most stable in the charge state q, and above which the defect is most stable in the charge state q'; $\epsilon(q/q')$ can be derived from the formation energies:

$$\epsilon(q/q') = \frac{E^f(D^q; E_F = 0) - E^f(D^{q'}; E_F = 0)}{(q' - q)}\,, \tag{3}$$

where $E_f(D^q; E_F = 0)$ is the defect formation energy of D^q when E_F is at the VBM ($E_F = 0$). The position of the transition level in the gap is independent of the choice of chemical potentials.

C. Chemical potentials

The formation energy of a defect depends explicitly on the chemical potentials μ_i, which are taken with respect to the total energy per atom of the standard phase for each species. For example, for the case of BSO, μ_{Ba} is referenced to the total energy of a Ba atom in crystalline (bcc) Ba metal, μ_{Sn} is referenced to crystalline (fcc) Sn metal, and μ_{O} to half of the total energy of an isolated $\mathrm{O_2}$ molecule. The chemical potentials are variables in

$BaSnO_3$		$SrSnO_3$		$CaSnO_3$	
Compound	ΔH_f	Compound	ΔH_f	Compound	ΔH_f
$BaSnO_3$	−11.45	$SrSnO_3$	−11.46	$CaSnO_3$	−11.82
Ba_2SnO_4	−17.01	Sr_2SnO_4	−16.97	Ca_2SnO_4	−17.17
BaO	−5.08	SrO	−5.63	CaO	−6.13
SnO_2	−5.27				
SnO	−2.54				

TABLE I: Calculated enthalpies of formation (ΔH_f, in eV) for various compounds used to determine the stability regions for $BaSnO_3$, $SrSnO_3$, and $CaSnO_3$, as described in the text. $\Delta H_f(SnO_2)$ and $\Delta H_f(SnO)$ are used in the determination of the stability region for all three stannates.

Eq. (1), and can be chosen to reflect experimental conditions during growth or annealing. Bounds can be placed on the range of chemical potentials by imposing the condition of stability of the parent compound, and to prevent formation of secondary phases. We illustrate this with the example of BSO, but the same approach applies to SSO and CSO.

The stability condition for BSO requires that the following equality holds:

$$\mu_{Ba} + \mu_{Sn} + 3\mu_O = \Delta H_f(BaSnO_3)\,. \qquad (4)$$

In order to prevent formation of bulk metallic phases, and to prevent loss of O_2, the chemical potentials are bounded from above,

$$\mu_{Ba}, \mu_{Sn}, \mu_O \leq 0\,. \qquad (5)$$

The chemical potentials are further restricted by the formation of other oxide phases, namely BaO, Ba_2SnO_4, SnO, and SnO_2:

$$\mu_{Ba} + \mu_O \leq \Delta H_f(BaO)\,, \qquad (6)$$
$$2\mu_{Ba} + \mu_{Sn} + 4\mu_O \leq \Delta H_f(Ba_2SnO_4)\,, \qquad (7)$$
$$\mu_{Sn} + \mu_O \leq \Delta H_f(SnO)\,, \qquad (8)$$
$$\mu_{Sn} + 2\mu_O \leq \Delta H_f(SnO_2)\,. \qquad (9)$$

In order to determine the range of relevant chemical potentials, enthalpies of formation for all the relevant compounds have been calculated within HSE; the values are listed in Table I. Using calculated values is most consistent in the context of using the chemical potentials for evaluating formation energies. We note that formation enthalpies calculated with HSE are generally close to experimental values; for example, we have calculated $\Delta H_f(BaO) = -5.08$ eV and $\Delta H_f(SnO_2) = -5.27$ eV, which compare well with the experimental values of $\Delta H_f(BaO) = -5.68$ eV and $\Delta H_f(SnO_2) = 5.99$ eV.[34]

By combining Eq. (4) with Eqs. (6) and (7) one obtains the following additional constraints in terms of μ_O and μ_{Sn},

$$\mu_{Sn} + 2\mu_O \geq \Delta H_f(BaSnO_3) - \Delta H_f(BaO)\,, \qquad (10)$$
$$\mu_{Sn} + 2\mu_O \geq 2\Delta H_f(BaSnO_3) - \Delta H_f(Ba_2SnO_4) \qquad (11)$$

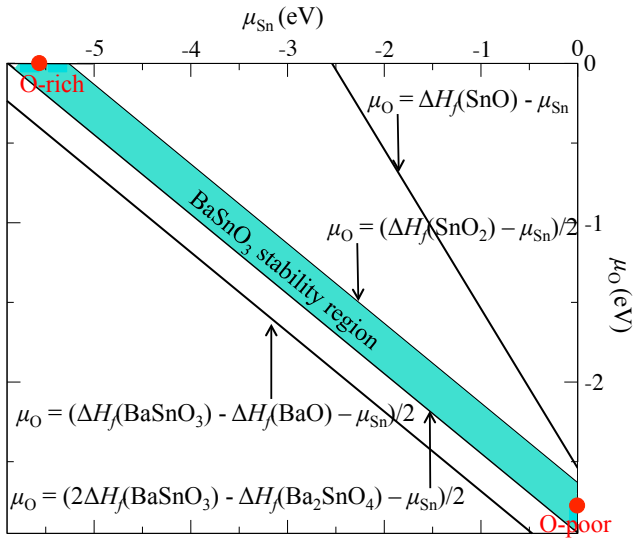

FIG. 1: Chemical stability region of $BaSnO_3$ plotted in the μ_{Sn}–μ_O plane. The shaded blue region indicates possible combinations of μ_O and μ_{Sn} for which $BaSnO_3$ is stable, and the corresponding value for μ_{Ba} is determined from Eq. (4). The red circles indicate the chemical potentials representing O-rich and O-poor conditions.

In this way, Eqs. (8)–(11) define the BSO stability region purely within the μ_{Sn}–μ_O plane; the range of chemical potentials for which BSO is stable is highlighted in Fig. 1. For a given μ_O, the stability region is quite narrow, and μ_{Sn} can only vary over a range of 0.62 eV. This allows us to focus on the dependence of formation energies on the oxygen chemical potential, since the allowed variation in the cation chemical potentials is relatively small. For the purposes of presenting our results, we will therefore focus on cation chemical potential values that correspond to the midpoint of the stability region, as we have done previously in the case of other perovskite oxides.[35] We will present results corresponding to extreme O-rich and O-poor growth conditions, corresponding to the points in the μ_{Sn}– μ_O plane indicated in Fig. 1. The corresponding value of μ_{Ba} is determined from Eq. (4). Subsequently, we will also explore the consequences of deviating from this midpoint, i.e., adopting more Ba-rich or Sn-rich conditions.

The same methodology is used to determine the appropriate chemical potentials for SSO and CSO. The enthalpies of formation used to calculate the SSO and CSO stability region are presented in Table I. A list of the chemical potentials used to represent O-rich and and O-poor conditions for BSO, SSO, and CSO is presented in Table II.

When considering La impurities, we also need to take into account limiting phases for La. In this case, μ_{La} is subject to the constraint $2\mu_{La} + 3\mu_O \leq \Delta H_f(La_2O_3)$; we have calculated $\Delta H_f(La_2O_3) = -17.67$ eV. Unless explicitly stated, we set μ_{La} to the maximum allowed

		Chemical potentials (eV)			
		μ_A	μ_{Sn}	μ_O	μ_{La}
BaSnO3	O-rich	-5.87	-5.58	0.00	-8.84
	O-poor	-3.08	0.00	-2.79	-4.65
SrSnO3	O-rich	-5.91	-5.55	0.00	-8.84
	O-poor	-3.14	0.00	-2.78	-4.67
CaSnO3	O-rich	-6.34	-5.48	0.00	-8.84
	O-poor	-3.60	0.00	-2.74	-4.73

TABLE II: Chemical potentials used to represent O-rich and O-poor growth conditions for the $ASnO_3$ perovskites (A = Ba, Sr, Ca).

		Lattice parameters (Å)			
		a	b	c	Ref.
$BaSnO_3$	Calc.	4.130	–	–	
	Exp.	4.119	–	–	[19]
$SrSnO_3$	Calc.	5.698	5.725	8.090	
	Exp.	5.708	5.704	8.066	[36]
$CaSnO_3$	Calc.	5.507	5.677	7.885	
	Exp.	5.532	5.681	7.906	[20]

TABLE III: Calculated lattice parameters for $BaSnO_3$, $SrSnO_3$, and $CaSnO_3$. Experimental values are listed for comparison.

value for a given μ_O, i.e., $\mu_{La} = (\Delta H_f(La_2O_3) - 3\mu_O)/2$, which corresponds to the most favorable conditions for La incorporation (i.e., the solubility limit). The effect of reducing μ_{La} is explored later in the manuscript.

III. RESULTS

A. Bulk properties

$BaSnO_3$ exhibits a high-symmetry cubic crystal structure [Fig. 2(a)]. Both SSO and CSO exhibit an orthorhombic crystal structure, characterized by tilting and rotation of the SnO_6 octahedra [Fig. 2(b)] in such a way that the cubic symmetry is broken, and the lattice is characterized by three lattice vectors a, b, and c, as shown in Fig. 2. Our calculated lattice parameters for BSO, SSO and CSO are compared with experimental values in Table III. The calculated pseudocubic lattice parameter of SSO is 4.04 Å, and that of CSO 3.95 Å, both significantly smaller than the 4.12 Å cubic lattice parameter of BSO.

The bulk electronic structure of the stannates is quite similar (see Refs.).[6,37,38] In each case, the VBM has mostly O $2p$ character, and the states around the CBM have mostly Sn $5s$ character. Given the spread in the reported values of band gaps for these stannates, we performed our HSE calculations with the standard value of the mixing parameter (α=0.25), resulting in calculated fundamental band gaps of 2.40 eV for BSO, 3.55 eV for SSO, and 4.31 eV for CSO. We have performed tests to check the sensitivity of our results to the value of the band gap. By increasing the mixing parameter to α=0.314, we obtain a band gap of 2.98 eV for BSO, close to the more reliable experimental values.[1,7] With the same mixing parameter we obain a band gap of 4.07 eV for SSO, close to the value of 4.10 eV reported in Ref.39. In Sec. III F we examine the sensitivity of our results to the choice of mixing parameter, finding that this does not affect our key conclusions.

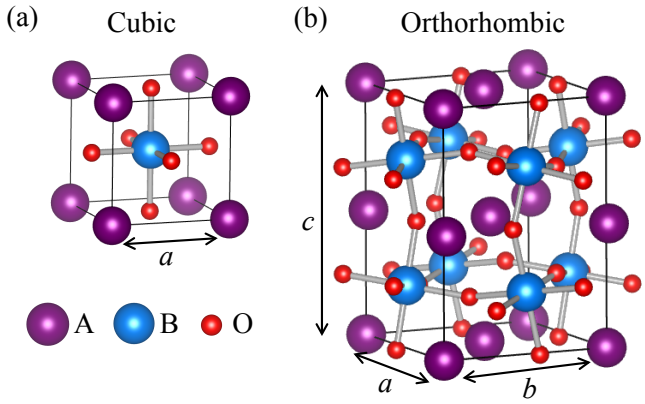

FIG. 2: (a) Cubic and (b) orthorhombic crystal structure for an ABO_3 perovskite. Purple spheres represent the A-site cation, blue spheres the B-site cation, and red spheres represent O atoms. $BaSnO_3$ adopts the cubic perovskite crystal structure, whereas $SrSnO_3$ and $CaSnO_3$ adopt an orthorhombic structure.

B. Lanthanum dopants

While La_{Ba} dopants act as shallow donors in BSO,[23] the nature of the donor state in SSO and CSO has not been explored. For donor-type defects, the formation energy of the positive charge state increases when the Fermi level increases according to Eq. (3). As a consequence, for wider-band-gap materials with high-lying conduction bands, the formation energy of the positive charge state can become very high when the Fermi level is near the CBM, and this tends to stabilize the neutral charge state, resulting in a $\epsilon(+/0)$ transition level below the CBM and the possibility of a deep donor level. Since the conduction bands of SSO and CSO are more than 1 eV higher in energy than that of BSO,[21] it is possible that La forms a deep-donor state in these materials.

We have calculated the La_A (A = Ba, Sr, Ca) $\epsilon(+/0)$

level for BSO, CSO and SSO, according to Eq. (3). As shown in Fig. 3, only the positive charge state of La_A is stable for any Fermi-level position in the gap, for all three materials. Indeed, we find that $\epsilon(+/0)$ is above the CBM for all three stannates, and therefore La_A impurities act as shallow donors that can freely contribute electrons to the conduction band. This result rules out poor thermal ionization of La impurities as the origin of the n-type doping difficulty in the wider gap stannates (SSO and CSO).

It is also possible that La impurities could self-compensate by occupying the Sn site, La_{Sn}, where they will act as acceptors. The results for formation energies are included in Fig. 3.

C. Native point defects

We will focus on the role of native point defects as compensating centers, thus limiting our study to defects that act as acceptors under n-type conditions. Oxygen interstitials (O_i) and A-on-Sn antisites (A_{Sn}) can in principle act as compensating acceptors; however, these defects are already known to have very high formation energies[23] and hence are not considered in this study. We thus focus on cation vacancies, and in particular on the fully ionized negative charge state that is most stable when the Fermi level is high in the band gap, i.e., $V_{Ba}^{-2}, V_{Sr}^{-2}, V_{Ca}^{-2}$, and V_{Sn}^{-4}. We acknowledge that these defects may assume other charge states when the Fermi level is lower in the gap,[23] but for the purposes of studying compensation of n-type doping it is sufficient to study the fully ionized charge states. The formation energies for the relevant native defect are shown in Fig. 3, for O-rich as well as O-poor conditions.

D. Compensation in $BaSnO_3$

For the case of BSO, La_{Ba} has a very low formation energy under both O-rich and O-poor conditions [Figs. 3(a) and (d)]. When BSO is doped with La, the presence of large concentrations of La_{Ba} donors drives the Fermi level toward the CBM; this increases the concentration of compensating acceptor-type defects, as their formation energy is lowered. Figure 3(d) shows that in the O-poor limit, the formation energy of La_{Ba} is much lower than that of any acceptor defects, and compensation will not be significant. Under O-rich conditions, however, the formation energy of La_{Ba} is shifted upward, and the formation energy of compensating acceptors is shifted downwards. In the O-rich limit, the formation energy of acceptor defects is comparable to, or even lower than that of La_{Ba} when the Fermi level is near the CBM, suggesting that severe compensation could occur. This indicates that such extreme oxygen-rich growth (or processing) conditions should be avoided.

We can develop more insight by evaluating the actual concentration of impurities, native point defects, and electrons in the conduction band. In Fig. 4(a) and (b) we plot these concentrations as a function of oxygen chemical potential, for Ba-rich [Eq. (11)] and Sn-rich [Eq. (9)] conditions. In these plots we assume that La is incorporated at the solubility limit; as explained in Sec. II C, this means that the La chemical potential (and the La concentration) change as a function of μ_O. (The dependence on μ_{La} will be examined in Sec. III G). Each combination of chemical potentials determines a set of formation energies [see Eq. (1) and Fig. 3], and the formation energies in turn yield concentrations [see Eq. (2)]. Both defect and electron concentrations depend on the temperature; we set $T = 1100$ K, which is within the typical range of growth temperatures for MBE and pulsed laser deposition.[14–16,18,40] The formation energies of charged species depend on the Fermi level, and the value of E_F in the system is determined by overall charge neutrality. For a doped n-type semiconductor this corresponds to setting to zero the net charge contributed by positively charged donors, negatively charged acceptors, and carriers in the conduction band. This value of the Fermi level (at T=1100 K) is also included in Fig. 4. The concentration of electrons in the conduction band is determined based on the Fermi-Dirac distribution and a conduction-band density of states, as in Ref..[6]

For BSO under Ba-rich conditions [Fig. 4(a)] the electron concentration is equal to the La_{Ba}^{+} concentration when $\mu_O < -1$ eV, i.e., there is no significant compensation. For larger μ_O values, however, compensation sets in, and for Ba-rich conditions this is mainly in the form of self-compensation by La_{Sn} acceptors. This leads to a rapid drop in the carrier concentration. Similar behavior is observed for Sn-rich conditions, but now compensation sets in as $\mu_O > -1.5$ eV, and V_{Ba} is the dominant compensating center. It is clear that higher carrier concentrations can be achieved under Sn-rich conditions, due to the fact that La_{Ba} has a lower formation energy (compared to Ba-rich conditions). Under all conditions, V_O has a very low concentration when doping with La_{Ba} is performed at the La solubility limit; the intentional doping with La increases the value of the Fermi energy, which increases the formation energy of V_O. In Sec. III G we will discuss what happens at lower La concentrations, where oxygen vacancies play a role.

Overall, we observe that Sn-rich and O-poor conditions are most conducive to achieving high n-type doping.

E. Compensation in $SrSnO_3$ and $CaSnO_3$

The issue of compensation becomes significantly more severe for the wider-band-gap stannates. Figure 3 shows that if the Fermi level is at the CBM, and for similar chemical potential conditions, the formation energy of compensating acceptors is much lower in SSO and CSO, when compared to BSO. With regard to chemical poten-

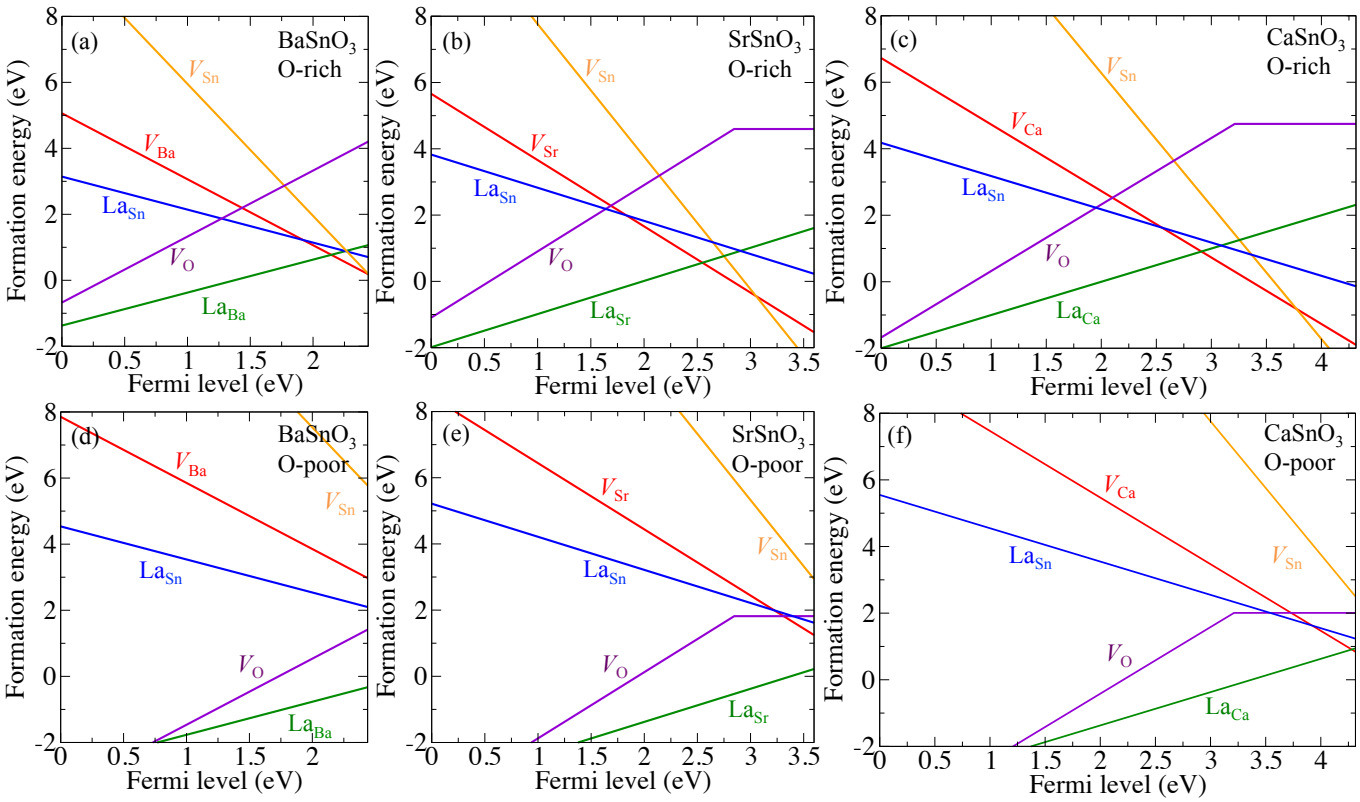

FIG. 3: Formation energies of point defects in perovskite stannates as a function of Fermi level. The top row shows defect formation energies under O-rich conditions for (a) $BaSnO_3$, (b) $SrSnO_3$, and (c) $CaSnO_3$; the bottom row shows defect formation energies under O-poor conditions for (d) $BaSnO_3$, (e) $SrSnO_3$, and (f) $CaSnO_3$. Chemical potential values are listed in Table II. The slope of each line segment indicates the stable charge state of the defect at a particular Fermi level, and kinks in the curves correspond to charge-state transition levels [Eq. (3)].

tial conditions, SSO and CSO exhibit the same trend as BSO: compensation is far worse in O-rich conditions than in O-poor conditions.

With respect to carrier and point-defect concentrations [Fig. 4], SSO and CSO exhibit the same key trends as BSO, however compensation is much worse. Under O-rich conditions the La_{Sn} acceptor is the dominant compensating center, at both the Sr-rich or Ca-rich limit, while under O-poor conditions the Sr-site or Ca-site vacancies dominate. The reader may wonder why Sn vacancies, which are shown in Fig. 3 to have the lowest formation energies under O-rich conditions when E_F is at the CBM, do not show up in Fig. 4 at all. The reason is that severe compensation sets in at Fermi levels well below the CBM, where V_{Sn}, particularly under Sn-rich conditions, has higher formation energies than the A-site vacancies.

As in BSO, the highest carrier concentrations in SSO and CSO can be achieved under Sn-rich and O-poor conditions. However, Fig. 4 shows that compensation is a more severe problem than in BSO. Doping CSO [Figs. 4(e)-(f)] looks particularly challenging. Under Ca-rich conditions, complete compensation occurs for all μ_O values; under Sn-rich conditions, a small degree of doping might be achieved under extreme O-poor conditions, but those are probably hard to achieve experimentally, and may lead to poor growth quality.

For SSO, Figs. 4(c) and (d) show that compensation is a concern, but that high electron concentrations (exceeding 10^{20} cm^{-3}) can be achieved by choosing O-poor and Sn-rich growth conditions.

F. Trends and the physics of compensation

Figures 3 and 4 clearly show that compensation of n-type dopants becomes more severe as we move from BSO to SSO to CSO, i.e., in the direction of increasing band gap. We can actually quantify this by relating the doping issues to the position of the conduction band in these materials.

Equation (1) shows that the formation energy of a negatively charged acceptor defect decreases as the Fermi level increases. Since the CBM of SSO and CSO lies more that 1 eV higher in energy than that of BSO,[21] E_F can rise to higher values in these materials, and conse-

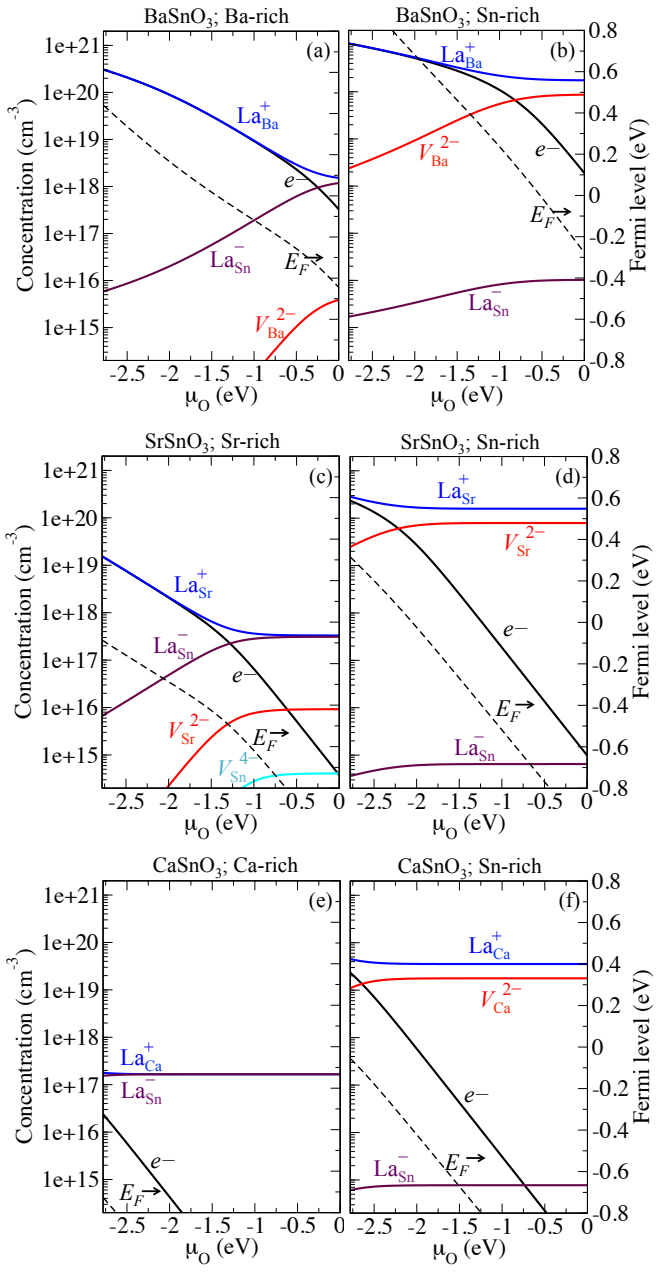

FIG. 4: Equilibrium concentrations of impurities, native defects and electrons (e^-) at T=1100 K as a function of the oxygen chemical potential μ_O, for (a)-(b) $BaSnO_3$, (c)-(d) $SrSnO_3$, and (e)-(f) $CaSnO_3$. The left panels (a),(c), and (f) are for the A-rich limits, the right panels (b), (d), and (f) for the Sn-rich limits. The corresponding values of the Fermi level are also included (dotted line, right axis); here the Fermi level is referenced to the conduction-band minimum.

quently the formation energy of acceptor defects can be substantially lower when the Fermi level approaches the CBM. In order to quantify this trend, we evaluate the equilibrium Fermi-level positions determined as in Fig. 4 under O-rich and O-poor conditions; for simplicity, we do not focus on A-rich vs. Sn-rich conditions but present the results for the midpoint of the stability region (i.e., for the chemical potentials listed in Table II). These Fermi-level positions are shown relative to the conduction-band edges in Fig. 5. In this plot, the band structures of BSO, SSO, and CSO are aligned according to the band offsets determined in Ref..[21]

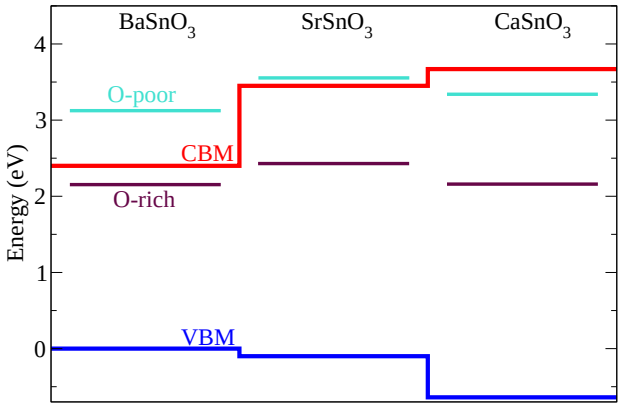

FIG. 5: Fermi level energies in La-doped $BaSnO_3$, $SrSnO_3$, and $CaSnO_3$, based on equilibrium between La donors, free electrons, and compensating acceptor defects. The band alignments are taken from Bjaalie *et al.*.[21] O-rich and O-poor conditions are shown; other chemical potentials are chosen as in Table II).

We observe that, on this absolute energy scale, the Fermi-level positions corresponding to specific chemical-potential conditions nearly line up for the three materials. This is consistent with established notions about relating doping problems to the position of band edges on an absolute energy scale.[24,41,42] When the plotted Fermi-level position is above the CBM, n-type doping is easily achievable. When the position is below the CBM, compensation is a problem, and it becomes more severe as the Fermi level moves deeper in the gap, as is the case for SSO and CSO compared to BSO.

We have examined the sensitivity of these results to the values of the band gaps in our HSE calculations, since our chosen value for the mixing parameter (α=0.25) likely underestimates the gaps. For CSO, our conclusion that the material cannot be n-type doped would only be strengthened if the band gap is larger than our calculated value of 4.31 eV. For BSO and SSO, as noted in Sec. III A, increasing the mixing parameter to α=0.314 leads to a band gap of 2.98 eV for BSO and 4.07 eV for SSO. We have recalculated the defect equilibria for BSO and SSO under O-rich and O-poor conditions with these larger band gaps; these tests indicate that our conclusions regarding the ability to dope these stannates under various conditions remain unaffected.

G. Dependence on dopant concentration

For purposes of the discussions in Secs. III C–III F, we assumed $\mu_{\rm La}$ was at the solubility limit. In Fig. 6, the concentration of impurities, native point defects, and electrons in the conduction band is plotted as a function of $\Delta\mu_{\rm La}$; higher $\Delta\mu_{\rm La}$ means higher doping, with $\Delta\mu_{\rm La} = 0$ corresponding to the solubility limit. Results are plotted for O-rich and O-poor conditions. Note that the solubility limit for La corresponds to $\mu_{\rm La} = [\Delta H_f({\rm La_2O_3}) - 3\mu_{\rm O}]/2$ (see Sec. II C), and since $\mu_{\rm O}$ is different for O-rich and O-poor conditions, the value of $\mu_{\rm La}$ corresponding to $\Delta\mu_{\rm La} = 0$ is different depending on whether the conditions are O-rich or O-poor. In Fig. 6 we assume that the chemical potentials for the cation and for Sn at the mid-point of the stannate stability region (Fig. 1).

For BSO under O-rich conditions [Fig. 6(a)] the electron concentration is negligible unless $\mu_{\rm La} > -1.5$ eV. Increasing $\Delta\mu_{\rm La}$ leads to an increase in the concentration of $\rm La_{Ba}$ donors, and the electron concentration increases. As the Fermi level rises, the concentration of compensating acceptors increases (with $V_{\rm Ba}$ dominating); for $\mu_{\rm La} > -1$ eV (La concentration around 10^{17} cm^{-3}), the electron concentration becomes lower than that of $\rm La_{Ba}$ donors. For the highest $\mu_{\rm La}$, the electron concentration rises to a maximum of around 10^{18} cm^{-3}.

Compensation is far less of a problem under O-poor conditions [Fig. 6(b)]. Here we observe that the free carrier concentration is about 4×10^{18} cm^{-3} even when $\mu_{\rm La}$ (and hence the La concentration) is negligibly low; this is due to the presence of oxygen vacancies ($V_{\rm O}$), which act as shallow double donors (hence the electron concentration is twice that of oxygen vacancies). We note that while our HSE calculations predict $V_{\rm O}$ to be a shallow donor, previous calculations using the PBE0 functional found $V_{\rm O}$ to be a deep donor with an ionization energy of 0.37 eV.[23] Experimentally, several groups have reported that $V_{\rm O}$ is shallow, since O-poor growth or annealing conditions lead to conductive material with high n-type carrier concentrations,[43–45] consistent with our results presented in Fig. 3 and Fig. 6. When $\mu_{\rm La} > -1.5$ eV, the $\rm La_{Ba}$ dopant takes over as the main donor, and the concentration of $V_{\rm O}$ is reduced [because their formation energy rises as the Fermi level is increased, see Fig. 3(d)]. Figure 6(b) shows that in the O-poor limit the electron concentration can increase to well above 10^{20} cm^{-3} near the La solubility limit, and compensation is not a problem.

Similar trends are observed for SSO [Figs. 6(c)–(d)] and CSO [Figs. 6(c)–(d)]: compensation becomes worse for high n-type doping, and can be suppressed by using O-poor growth conditions. Our results show that doping of CSO will be extremely difficult, if not impossible. For SSO, we find that oxygen-rich growth conditions lead to very severe compensation, but that compenstation can be completely suppressed under O-poor conditions, and carrier concentrations close to 10^{20} cm^{-3} should be achievable. In addition, by pushing the Sn:Sr ratio towards the Sn-rich limit [see Sec. III E and Fig. 4(d)]) carrier concentrations in excess of 10^{20} cm^{-3} can be achieved.

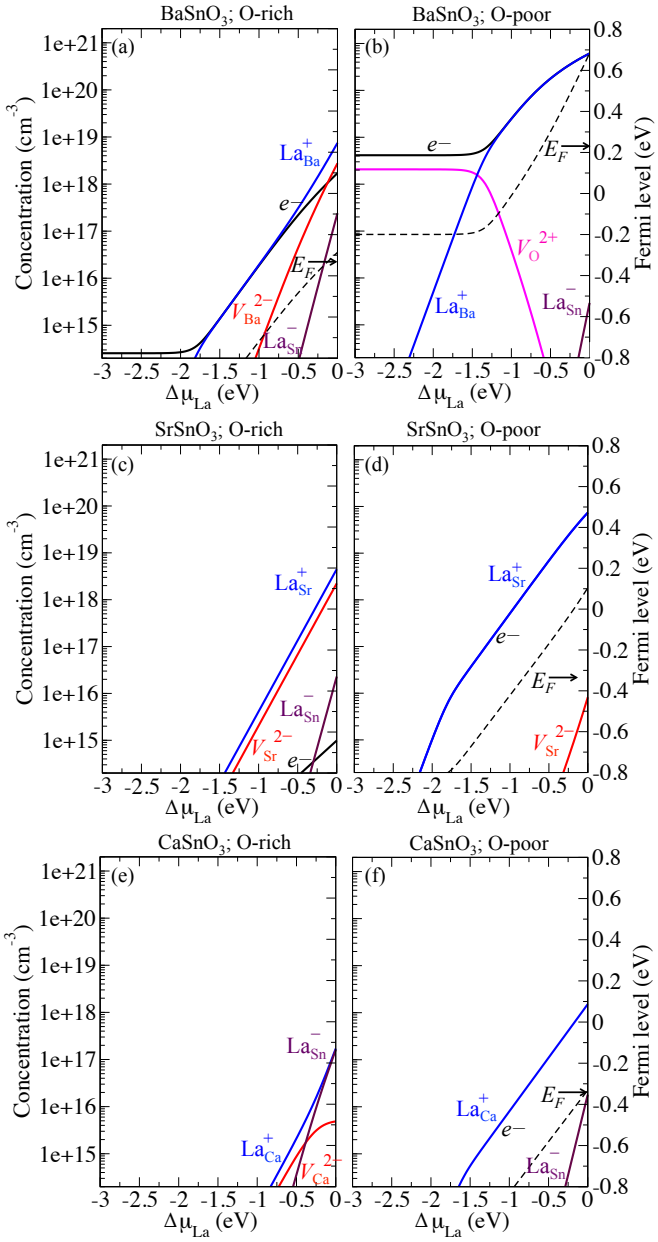

FIG. 6: Equilibrium concentrations of impurities, native defects and electrons (e^-) at T=1100 K as a function of $\Delta\mu_{\rm La}$ (as defined in the text), for (a)-(b) $BaSnO_3$, (c)-(d) $SrSnO_3$, and (e)-(f) $CaSnO_3$. The left panels (a),(c), and (f) are for the O-rich limits, the right panels (b), (d), and (f) for the O-poor limits. The corresponding values of the Fermi level are also included (dotted line, right axis); here the Fermi level is referenced to the conduction-band minimum.

H. Comparison with experiment

Our results for the formation of compensating acceptor defects in BSO shed light on recent experimental work. Prakash *et al.*[16] grew La-doped BSO by MBE and studied the carrier concentration and mobility as a function of the cation beam-equivalent pressure. Outside of a narrow growth window, the carrier concentration and mobility were strongly reduced by deviation from cation stoichiometry, consistent with the formation of compensating acceptors. Based on the results presented in Fig. 4, the dominant compensating centers are likely to be La_{Sn} under Ba-rich conditions, and V_{Ba} under Sn-rich conditions. The comparison between Figs. 4(a) and (b) indicates that deviating towards Ba-rich conditions has a more severe impact on carrier concentrations than deviating towards Sn-rich; this is because, in addition to leading to compensation by La_{Sn} acceptors, Ba-rich conditions make it more difficult for La to incorporate on the Ba site. These trends are entirely consistent with the results presented in Fig. 5(c) of Ref.16, where it was shown that deviating from an optimal Sn:Ba ratio causes a more severe decline in carrier concentrations on the low Sn:Ba side (i.e., Ba-rich conditions).

Schumann *et al.*[18] found that La-doped BSO grown by MBE was n-type with a high carrier concentration, whereas SSO grown by the same methodology was insulating. Our Figure 5 explains why La-doped BSO and SSO grown under similar conditions can have such disparate electrical properties. The higher lying conduction band of SSO leads to an increased tendency for charge compensation by formation of acceptor defects. Despite the doping difficulty, we point out that our calculations predict that $SrSnO_3$ *can* in principle be doped n-type, although conditions should be closer to O-poor conditions to achieve high n-type doping. Recent experiments by Wang *et al.* confirm that high n-type doping levels can be achieved in SSO[46]; in these experiments the authors found that deviations in the cation stoichiometry lead to a significant reduction in the n-type carrier concentration and mobility, consistent with charge compensation.

Post-growth annealing of thin films in an O-rich environment has sometimes been performed with the intent of removing oxygen vacancies.[40] Our results indicate that such annealing could actually promote the formation of compensating acceptor defects. However, this would depend on the kinetics of the relevant defect; it seems more likely that native vacancy defects could spontaneously form compared to La_{Sn}. Based on our results, we suggest growth or annealing conditions closer to O-poor where possible, in order to achieve optimum doping in the perovskite stannates.

IV. SUMMARY

We have performed first-principles calculations to investigate the origin of the n-type doping difficulty in the perovskite stannates $ASnO_3$, where A is Ba, Sr, or Ca. In all cases, La impurities form a shallow donor state by substituting at the A-cation site. However, depending on the growth (or annealing) conditions, these La donors will be compensated by the formation of acceptor defects. We find that O-poor growth conditions are most favorable for n-type doping; compensation becomes more of a problem under O-rich conditions. The dominant compensating center depends on whether the growth is Sn-rich or A-rich: La_{Sn} acceptors dominate under A-rich conditions, while A-site vacancies dominate under Sn-rich conditions.

Compensation is more of a problem for the wider band-gap stannates, SSO and CSO, and we quantitatively correlate this with the energetically higher lying conduction-band edge. Our results show that n-type doping of CSO will probably not be possible, but SSO can be n-type under the right growth conditions. Our diagrams as a function of chemical potentials provide a guide for selecting optimum growth or annealing conditions that will achieve high n-type doping and suppress compensation.

Acknowledgments

We acknowledge useful discussions with T. Schumann, S. Stemmer, B. Jalan and D. G. Schlom. This work was supported in part by the Center for Low Energy Systems Technology (LEAST), one of the six SRC STARnet Centers, sponsored by MARCO and DARPA, and by the NSF MRSEC program (DMR-1121053). Computational resources were provided by the Extreme Science and Engineering Discovery Environment (XSEDE), supported by NSF (ACI1053575), and the Center for Scientific Computing at the CNSI and MRL (an NSF MRSEC, DMR-1121053) (NSF CNS-0960316).

[1] H. J. Kim, U. Kim, T. H. Kim, J. Kim, H. M. Kim, B.-G. Jeon, W.-J. Lee, H. S. Mun, K. T. Hong, J. Yu, et al., Phys. Rev. B **86**, 165205 (2012).
[2] X. Luo, Y. S. Oh, A. Sirenko, P. Gao, T. Tyson, K. Char, and S.-W. Cheong, Appl. Phys. Lett. **100**, 172112 (2012).
[3] H. J. Kim, U. Kim, H. M. Kim, T. H. Kim, H. S. Mun, B.-G. Jeon, K. T. Hong, W.-J. Lee, C. Ju, K. H. Kim, et al., Appl. Phys. Express **5**, 061102 (2012).
[4] K. Krishnaswamy, L. Bjaalie, B. Himmetoglu, A. Janotti, L. Gordon, and C. G. Van de Walle, Appl. Phys. Lett. **108**, 083501 (2016).
[5] B. Himmetoglu, A. Janotti, H. Peelaers, A. Alkauskas, and C. G. Van de Walle, Phys. Rev. B **90**, 241204 (2014).
[6] K. Krishnaswamy, B. Himmetoglu, Y. Kang, A. Janotti,

and C. G. Van de Walle, Phys. Rev. B **95**, 205202 (2017).
[7] S. A. Chambers, T. C. Kaspar, A. Prakash, G. Haugstad, and B. Jalan, Appl. Phys. Lett. **108**, 152104 (2016).
[8] S. Xing, C. Shan, K. Jiang, J. Zhu, Y. Li, Z. Hu, and J. Chu, J. Appl. Phys. **117**, 103107 (2015).
[9] H. Y. Hwang, Y. Iwasa, M. Kawasaki, B. Keimer, N. Nagaosa, and Y. Tokura, Nat. Mater. **11**, 103 (2012).
[10] Y. Tokura and H. Y. Hwang, Nat. Mater. **7**, 694 (2008).
[11] U. Kim, C. Park, T. Ha, Y. M. Kim, N. Kim, C. Ju, J. Park, J. Yu, J. H. Kim, and K. Char, APL Mater. **3**, 036101 (2015).
[12] C. Park, U. Kim, C. J. Ju, J. S. Park, Y. M. Kim, and K. Char, Appl. Phys. Lett. **105**, 203503 (2014).
[13] B. Hadjarab, A. Bouguelia, A. Benchettara, and M. Trari, J. Alloys Compd. **461**, 360 (2008).
[14] U. Kim, C. Park, T. Ha, R. Kim, H. S. Mun, H. M. Kim, H. J. Kim, T. H. Kim, N. Kim, J. Yu, et al., APL Materials **2**, 056107 (2014).
[15] S. Yu, D. Yoon, and J. Son, Appl. Phys. Lett. **108**, 262101 (2016).
[16] A. Prakash, P. Xu, X. Wu, G. Haugstad, X. Wang, and B. Jalan, J. Mater. Chem. C **5**, 5730 (2017).
[17] H. Mun, U. Kim, H. Min Kim, C. Park, T. Hoon Kim, H. Joon Kim, K. Hoon Kim, and K. Char, Appl. Phys. Lett. **102**, 252105 (2013).
[18] T. Schumann, S. Raghavan, K. Ahadi, H. Kim, and S. Stemmer, J. Vac. Sci. Technol. **34**, 050601 (2016).
[19] A.-M. Azad and N. C. Hon, Journal of Alloys and Compounds **270**, 95 (1998).
[20] A. Vegas, M. Vallet-Regi, J. González-Calbet, and M. Alario-Franco, Acta Crystallogr. Sect. B-Struct. Sci. **42**, 167 (1986).
[21] L. Bjaalie, B. Himmetoglu, L. Weston, A. Janotti, and C. G. Van de Walle, New J. Phys. **16**, 025005 (2014).
[22] E. Baba, D. Kan, Y. Yamada, M. Haruta, H. Kurata, Y. Kanemitsu, and Y. Shimakawa, Journal of Physics D: Applied Physics **48**, 455106 (2015).
[23] D. O. Scanlon, Phys. Rev. B **87**, 161201 (2013).
[24] C. Freysoldt, B. Grabowski, T. Hickel, J. Neugebauer, G. Kresse, A. Janotti, and C. G. Van de Walle, Rev. Mod. Phys. **86**, 253 (2014).
[25] J. Heyd, G. E. Scuseria, and M. Ernzerhof, J. Chem. Phys. **118**, 8207 (2003).
[26] J. Heyd and G. E. Scuseria, J. Chem. Phys. **121**, 1187 (2004).
[27] G. Kresse and J. Furthmüller, Phys. Rev. B **54**, 11169 (1996).
[28] J. P. Perdew, K. Burke, and M. Ernzerhof, Phys. Rev. Lett. **77**, 3865 (1996).
[29] A. V. Krukau, O. A. Vydrov, A. F. Izmaylov, and G. E. Scuseria, J. Chem. Phys. **125**, 224106 (2006).
[30] J. Perdew, M. Ernzerhof, and K. Burke, J. Chem. Phys. **105**, 9982 (1996).
[31] P. E. Blöchl, Phys. Rev. B **50**, 17953 (1994).
[32] C. Freysoldt, J. Neugebauer, and C. G. Van de Walle, Phys. Rev. Lett. **102**, 016402 (2009).
[33] C. Freysoldt, J. Neugebauer, and C. G. Van de Walle, Phys. Status Solidi B **248**, 1067 (2011).
[34] P. J. Linstrom and W. Mallard (2001).
[35] L. Weston, A. Janotti, X. Y. Cui, C. Stampfl, and C. G. Van de Walle, Phys. Rev. B **89**, 184109 (2014).
[36] P. S. Beurmann, V. Thangadurai, and W. Weppner, J. Solid State Chem. **174**, 392 (2003).
[37] H. Chen and N. Umezawa, Int. J. Photoenergy **2014** (2014).
[38] W. Zhang, J. Tang, and J. Ye, J. Mater. Res. **22**, 1859 (2007).
[39] H. Mizoguchi, H. W. Eng, and P. M. Woodward, Inorg. Chem. **43**, 1667 (2004).
[40] S. Raghavan, T. Schumann, H. Kim, J. Y. Zhang, T. A. Cain, and S. Stemmer, APL Mater. **4**, 016106 (2016).
[41] S. Zhang, S.-H. Wei, and A. Zunger, Physica B **273**, 976 (1999).
[42] W. Walukiewicz, Physica B **302**, 123 (2001).
[43] Q. Liu, J. Dai, Y. Zhang, H. Li, B. Li, Z. Liu, and W. Wang, J. Alloys Compd. **655**, 389 (2016).
[44] H. I. Jaim, S. Lee, X. Zhang, and I. Takeuchi, Appl. Phys. Lett. **111**, 172102 (2017).
[45] I. A. Alagdal and A. R. West, J. Mater. Chem. C **4**, 4770 (2016).
[46] T. Wang, L. R. Thoutam, A. Prakash, W. Nunn, G. Haugstad, and B. Jalan, Phys. Rev. Materials **1**, 061601 (2017).